JMEPEG (2012) 21:1824–1840
DOI: 10.1007/s11665-011-0069-z

1059-9495/$19.00

# Computational Analysis of Material Flow During Friction Stir Welding of AA5059 Aluminum Alloys

*M. Grujicic, G. Arakere, B. Pandurangan, J.M. Ochterbeck, C-F. Yen, B.A. Cheeseman, A.P. Reynolds, and M.A. Sutton*

*(Submitted July 13, 2011)*

**Workpiece material flow and stirring/mixing during the friction stir welding (FSW) process are investigated computationally. Within the numerical model of the FSW process, the FSW tool is treated as a Lagrangian component while the workpiece material is treated as an Eulerian component. The employed coupled Eulerian/Lagrangian computational analysis of the welding process was of a two-way thermo-mechanical character (i.e., frictional-sliding/plastic-work dissipation is taken to act as a heat source in the thermal-energy balance equation) while temperature is allowed to affect mechanical aspects of the model through temperature-dependent material properties. The workpiece material (AA5059, solid-solution strengthened and strain-hardened aluminum alloy) is represented using a modified version of the classical Johnson-Cook model (within which the strain-hardening term is augmented to take into account for the effect of dynamic recrystallization) while the FSW tool material (AISI H13 tool steel) is modeled as an isotropic linear-elastic material. Within the analysis, the effects of some of the FSW key process parameters are investigated (e.g., weld pitch, tool tilt-angle, and the tool pin-size). The results pertaining to the material flow during FSW are compared with their experimental counterparts. It is found that, for the most part, experimentally observed material-flow characteristics are reproduced within the current FSW-process model.**

**Keywords** friction stir welding, material-flow simulation and analysis, process modeling

## 1. Introduction

Friction stir welding (FSW) is a relatively new solid-state material joining process which was invented at The Welding Institute, Cambridge, UK in 1991 by Thomas (Ref 1). Within this joining process, a non-consumable hard-material welding tool is used to generate (via frictional-sliding and plastic-work dissipation) sufficient amount of heat, in the workpiece material surrounding the tool/workpiece interface, required for successful welding. A detailed description/analysis of the FSW process could be found in the seminal work by W. M. Thomas and co-workers (Ref 1, 2) and, hence, will not be provided in this article.

While it has been demonstrated that a number of metallic and polymeric materials can be joined using FSW, the industrial interest has been primary in the welding of aluminum alloys. For a wide variety of aluminum-alloy grades (even for those previously considered as unweldable), it was clearly demonstrated that high-quality/defect-free/high-strength FSW joints (in a 1-50 mm thickness range) can be produced. The additional, often-cited advantage of FSW is its ability to be carried out in various positions (e.g., horizontal, vertical, overhead, orbital, etc.). In regard to different weld designs, FSW is most often used (but is not limited) in the production of butt and lap joints.

It has been generally established that the FSW-tool design is an important FSW process parameter affecting all aspects of the joining process (e.g., temporal evolution and spatial distribution of the material and heat transport/flow, material microstructure and properties, the presence/absence of weld flaws/defects, etc.). Typically, an FSW-tool consists of three main sections, Fig. 1 (a) shank; (b) shoulder; and (c) pin. Furthermore, the FSW process is generally carried out using a conventional milling machine, within which the FSW-tool is rotated about its (longitudinal) axis, while the workpiece is held in place using a fixturing device. The main role of the shank is to provide a connection to the milling machine spindle and, thus, to apply a torque to the FSW-tool. The primary role of the tool shoulder is to apply the required level of the downward contact pressure onto the workpiece, facilitate generation of the heat and ensure efficient stirring of the material and to confine the thermally softened workpiece material and prevent its escape from the weld region. To ensure the desired level of the tool-shoulder functionality, the bottom face of the shoulder generally possesses an upright truncated-conical profile as well as scrolls/spirals. As far as the pin is concerned, its main role is to provide an additional contribution to the heat generation (via frictional-sliding and plastic-work dissipation) and to ensure efficient and thorough mixing of the workpiece material in the longitudinal, transverse, and vertical directions. To improve the functionality of the FSW-tool, the pin is often tapered and contains external features such as threads, flutes, flats, etc. Since the extents of material mixing and heating below the tool-pin are quite low and mainly localized in a thin region adjacent

**M. Grujicic, G. Arakere, B. Pandurangan,** and **J.M. Ochterbeck**, Department of Mechanical Engineering, Clemson University, 241 Engineering Innovation Building, Clemson, SC 29634-0921; **C-F. Yen** and **B.A. Cheeseman**, Army Research Laboratory—Survivability Materials Branch, Aberdeen, Proving Ground, MD 21005-5069; and **A.P. Reynolds** and **M.A. Sutton**, Department of Mechanical Engineering, University of South Carolina, Columbia, SC 29208. Contact e-mail: gmica@clemson.edu.

to the pin bottom, the length of the pin is generally chosen in such a way that it extends to a depth very close to the workpiece bottom face. This ensures that the FSW weld is complete and defect free.

A schematic of a typical FSW set-up used in the fabrication of butt-joints is displayed in Fig. 2. The FSW fabrication of butt-joints generally involves the following steps: (a) The workpiece components with mating surfaces are subjected to high contact pressures and secured to a rigid backing plate using a fixturing device. This prevents potential separation, sliding, or lifting of the workpiece components and enables positioning of the work-piece material at an angle relative to the tool longitudinal axis; (b) The welding tool secured within the milling machine tool holder is spun to the desired rotational speed and is slowly plunged into the workpiece components contact-interface region until the tool shoulder contacts (and slightly indents) the work-piece upper surface and the lowest point of the pin is very near the workpiece back face; (c) The rotating tool is then forcibly advanced along the workpiece components contact interface while the workpiece material is stirred, extruded around the tool, and subsequently forged in the wake of the tool; and (d) At the completion of the welding process, the tool advancement is terminated and the tool is retracted (i.e., pulled out of the workpiece) while, the tool continues to rotate. Once the tool is fully retracted, the spindle rotation is terminated and the weldment is removed from the fixturing device. Clearly, a hole (which needs to be eliminated) is left in the weldment upon retraction of the FSW tool.

Since the FSW tool rotates in the same (clockwise or counterclockwise) direction during welding, the thermo-mechanical and microstructural fields associated with the FSW process are not symmetric. Consequently, the side of the weld on which the tangential component of the rotational velocity and the translational velocity of the FSW tool are of the same sense is commonly referred to as the *advancing side* while the other side of the weld is called the *retreating side*. In addition, the following terms are often used to denote various regions of the weld relative to the position of the tool: (a) Regions ahead and behind the tool are referred to as the *leading* and *trailing sides*, respectively; and (b) the top and bottom of the weld are denoted as the *crown* and *root*, respectively.

FSW normally involves complex interactions and competition between various mass and heat transport phenomena, plastic deformation and damage/fracture mechanisms, and microstructure evolution processes (Ref 3-10). Consequently, the material microstructure (and mechanical properties) in the weld region are highly complex and spatially diverse. Metallographic examinations of the FSW joints typically reveal the existence of the following four weld zones (not counting the unaffected/base-metal zone which is far enough from the weld so that material microstructure/properties are not altered by the joining process) (Fig. 3) (a) the heat-affected zone (HAZ) in which material microstructure/properties are effected only by the thermal effects associated with FSW. While this zone is normally found in the case of fusion-welds, the nature of the

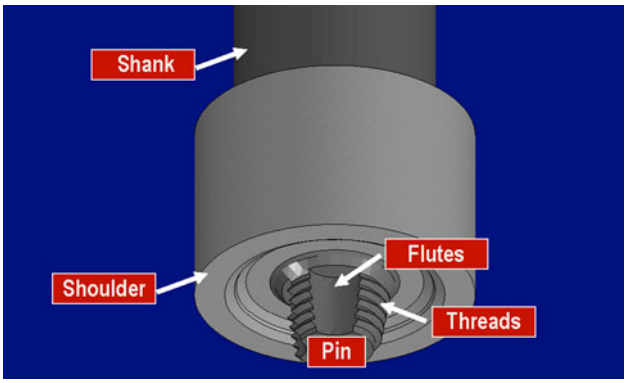


**Fig. 1** Typical friction stir welding (FSW) tool used for joining of aluminum alloys

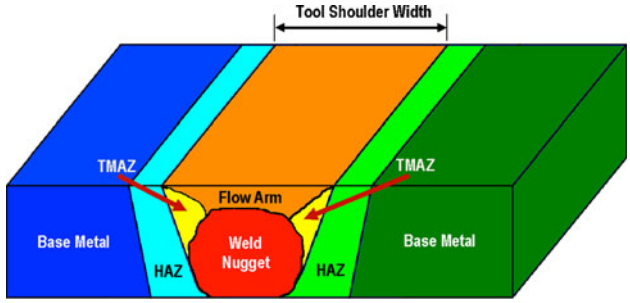


**Fig. 3** A schematic of the main microstructural zones associated with the typical FSW joint

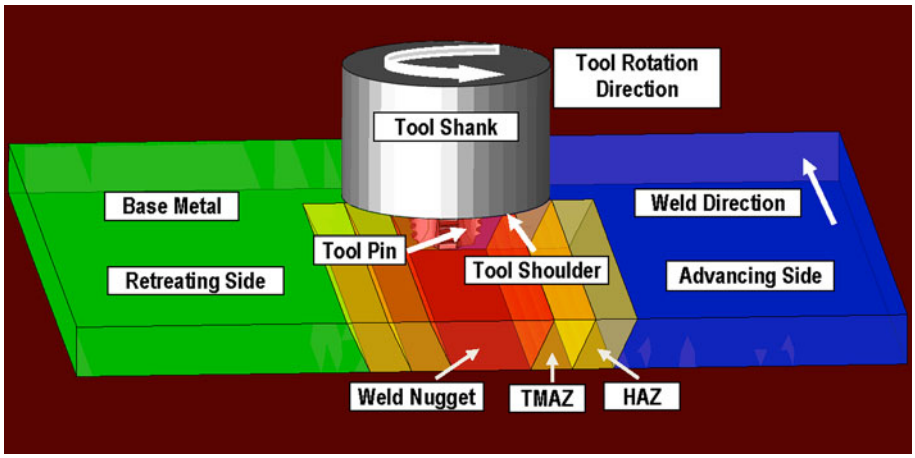


**Fig. 2** A schematic of the friction stir welding (FSW) process

microstructural changes (e.g., recovery, recrystallization, grain growth, precipitate coarsening, precipitate dissolution, etc., depends on the workpiece material chemical composition and microstructural state) may be different in the FSW case due to generally lower temperatures and a more diffuse heat source; (b) the thermo-mechanically affected zone (TMAZ) is located closer than the HAZ to the workpiece components contact interface. Consequently, both the thermal and the mechanical aspects of the FSW process affect the material microstructure/properties in this zone. While the original grains are retained in this zone they experience a considerable amount of plastic deformation during the FSW process. Consequently, it is often observed (using metallographic analysis of the transverse and horizontal weld sections) that the grains have been subjected to bending; (c) the weld *nugget* is the innermost zone of an FSW joint. As a result of the way the material is transported from the regions ahead of the tool to the wake regions behind the tool, this zone typically contains the so called onion-ring features. The material in this region has been subjected to most severe conditions of plastic deformation and high-temperature exposure and consequently contains a very-fine dynamically recrystallized (equiaxed grain microstructure) weld microstructure. The width of the nugget is slightly larger than the FSW-tool pin diameter; and (d) the last FSW zone which is located above the weld nugget is generally referred to as the *flow arm*. This weld zone typically contains the workpiece material which was (during welding) temporarily confined by the upright truncated-conical profile of the FSW-tool shoulder underside.

When compared to the conventional fusion-welding processes, FSW offers a number of advantages. Since a fairly detailed account of these advantages can be found in our recent work (Ref 11), a similar detailed account of these advantages will not be presented here. Nevertheless, it should be noted that most of these advantages are due to the fact that FSW is associated with lower temperatures, does not involve fusion and re-solidification of the workpiece material and that no filler metal, flux or fuel/oxidizer are used. Consequently, the extents of microstructural changes and the associated material property degradation are smaller relative to their counterparts observed in the conventional fusion-based welding processes.

Despite the fact that FSW is a relatively new joining technology, it has already found a fairly wide-scale application in several industries. Among the most notable examples of the successful deployment of the FSW process for the fabrication of high-performance/cost-effective structures are: (a) Large-scale production of aluminum FSW-joined ferryboat deck structures in Finland; (b) manufacture of Al-Mg-Si-based alloy FSW-joined bullet-train cabins in Japan; (c) fabrication of Al-Cu-based alloy FSW-joined rocket launch systems by Boeing; (d) replacement of the conventional fusion welding processes with FSW in the manufacture of Al-Li alloy-based space-shuttle external fuel-tanks by NASA; and (e) application of FSW in highly demanding jet engine applications by General Electric.

Over the last two decades, considerable experimental research efforts have been invested toward obtaining a better understanding of the FSW joining mechanism and the accompanying evolution of the welded-materials microstructure/properties (e.g., Ref 12-15) as well as to rationalizing the effect of various FSW process parameters on the weld quality/integrity (e.g., Ref 12, 16-19). In the same time period, physically based modeling and simulations of the FSW process have also been given considerable attention (e.g., Ref 20-23). A critical assessment of the past experimental and computational approaches revealed that the majority of these were concerned with important practical issues such as the development of tools and identification of the optimum FSW-process parameters for a variety of alloys and understanding the development and characterization of the weld-material microstructure/properties. The phenomenon of workpiece material flow, despite its major role in the formation, structural integrity, and the overall properties of the weld, has been given considerably less attention. As a main objective of the present work, an attempt is made to address (computationally) this short coming. In particular, it is argued that any numerical model for the FSW-process to be considered reliable and of high-fidelity must correctly predict the essential features of the material flow (as established using various experimental means, section 2).

The organization of this article is as follows: A concise overview of the major experimental FSW flow-visualization techniques and findings has been presented in section 2. A brief description of the combined Eulerian/Lagrangian fully coupled thermo-mechanical model and computational analysis of the FSW process is provided in section 3. The key computational results pertaining to the material flow during the FSW process are presented and compared with their respective experimental counterparts in section 4. The main conclusions resulting from the present study are summarized in section 5.

## 2. Material Flow Visualization During FSW

In this section, a brief overview is provided of the main FSW flow experimental-visualization studies carried out over the past decade. One of the first FSW-flow experimental-visualization studies was conducted by Midling (Ref 24) who investigated the effect of the FSW tool traverse velocity on the workpiece material flow (as revealed by spatial distribution of the material interfaces within the weld) in dissimilar-material FSW joints. This procedure, however, provided only limited insight into the workpiece material flow since it relied on the visualization of the dissimilar alloys interfaces alone.

Li et al. (Ref 25) carried out a series of FSW experiments involving either dissimilar aluminum-alloy grades or aluminum/copper workpiece materials. By analyzing material patterns seen in the weld metallographic cross sections of the FSW welds, Li et al. established that the resulting workpiece material flow is of a chaotic nature.

A major step forward in the visualization of the material flow was made in the work of Colligan (Ref 26), who employed a technique in which small-diameter steel spheres were placed at different positions along the workpiece components contact interface before welding and their final positions within the weld were determined by radiographing the post-welded structures. The main findings of Colligan (Ref 26) can be summarized as follows: (a) The workpiece material is stirred (via chaotic-mixing) only in the upper portion of the weld; and (b) in the remaining portions of the weld material flow involves only extrusion of the material around the rotating FSW tool. The main limitations of Colligan's work are: (a) FSW-flow visualization was inferred by tracking only single points (i.e., the center of gravity of undeformed steel spheres); and (b) the chaotic-mixing observed might have been caused by the presence of finite-size spheres which act not only as flow-field markers but also cause changes/disruptions in the material flow.

In addition, since the details of the material flow are significantly affected by the FSW tool geometry and other FSW process parameters, the findings of Colligan (Ref 26) could not be readily generalized.

The next major step forward in the visualization of the material flow was made in a series of papers by Reynolds and co-workers (Ref 27-30) who introduced the so-called marker insert technique. Within this technique, markers of a different aluminum-alloy grade are inserted along and on both sides of an aluminum-alloy workpiece contacting interface (i.e., in the path of a rotating and traversing FSW tool). The final position and shape of the markers were determined by: (a) Milling-off successive 0.25 mm thick slices from the top surface of the weldment; (b) etching each newly created top surface of the weldment using an etchant which produces a strong contrast between the two aluminum-alloy grades; (c) capturing a digital image of each etched weldment top surface; (d) digital image analysis of each etched weldment top surface; and (e) assembly of the individual images to form a complete three-dimensional model for the FSW weldment revealing the position and the deformed shape of the markers. These findings are subsequently used to infer the essential features of material flow during the FSW process.

The main findings obtained by Reynolds and co-workers (Ref 27-30) can be summarized as follows: (a) The material flow during FSW is influenced by both the translational and rotational components of the FSW tool motion; (b) the main component of the material flow is in the horizontal plane and in a general direction which is opposite to the direction of FSW tool travel and involves material motion/extrusion around the tool and its placement in a region behind the tool. In this case, the tool shoulder, the pin, the backing plate, and the base-metal portion of the workpiece material effectively form an extrusion die; (c) workpiece material stirring (i.e., its rotational motion around the tool longitudinal axis) occurs predominantly in the top portion of the weld in which the rotating action of the tool shoulder causes material transport from the retreating to the advancing side of the weld; (d) the material transferred from the retreating to the advancing side interferes with the extrusion (in the horizontal plane) of the advancing-side material in the path of FSW-tool pin. This results in a downward (out-of-plane) component of the material extrusion direction. The downward motion of the extruded material extends through the thickness of the workpiece material on the advancing side till the weld root at which point, due to the presence of the rigid backing plate, the extruded material crosses over to the retreating side and begins its ascent (i.e., to move in the upward direction). As a consequence, the material acquires a rotational motion around the longitudinal axis of the weld; (e) the extent of the vertical circular motion described in (d) increases with a reduction in the value of the weld-pitch which is attributed to the auguring effect of the threaded FSW-tool pin; and (f) the extent of vertical rotation also increases with the pin diameter and this effect is attributed to the associated increase in the amount of energy transferred into the weld by the FSW tool.

## 3. FSW Computational Modeling and Analysis

Modeling of the FSW process was carried out in our prior work using an Arbitrary Lagrangian Eulerian (ALE) fully coupled thermo-mechanical finite-element procedure (Ref 20-22). The main emphasis of our prior work was the prediction of microstructure and property fields within the weld region in a variety of solid-solution strengthened and age-hardened aluminum- and titanium-based alloys. Since the main emphasis of the present work is the analysis of the material flow during the FSW process under different tool-design and process-parameter conditions, a new Combined Eulerian Lagrangian (CEL) fully coupled thermo-mechanical analysis of the FSW process is introduced. While this analysis is usually computationally more expensive than the corresponding ALE analysis, it is generally found to be more robust and more suitable for studying material-mixing processes. It should be recognized, however, that the ALE and CEL analyses share many features. Hence, the features common to the two analyses will only be discussed briefly here.

### 3.1 FSW Computational Analysis

**3.1.1 Computational Domain.** The computational domain used consists of two separate sub-domains, one of an Eulerian-type and the other of a Lagrangian-type. The Eulerian sub-domain (used to model the workpiece) is of a parallelepiped shape with the dimensions of $L \times W \times H = 50 \times 40 \times 8$ mm, respectively. This sub-domain is typically discretized using Eulerian 8-node brick elements with a characteristic edge length of 0.44 mm. The Lagrangian sub-domain is used to model the FSW tool. As will be discussed in section 4, a prototypical FSW tool design consisting of a tapered threaded pin and a cylindrical shoulder with an upright truncated conical under-cut was utilized in the present work. The tools are meshed using 4-node tetrahedron continuum elements. Examples of the Eulerian and Lagrangian sub-domains used in the present work are displayed in Fig. 4. It should be noted that in this figure, for clarity, the tool is shown in the retracted position. In the present work, the Eulerian sub-domain typically consisted of 150,000 elements while the tool contained 20,000 elements.

**3.1.2 Computational Analysis Type.** The FSW process is analyzed computationally using a Combined Eulerian Lagrangian and a fully coupled thermo-mechanical finite-element algorithm. Within this algorithm, heat dissipation associated with plastic deformation and tool/workpiece interfacial friction-sliding is treated as a heat-source in the governing thermal equation. On the other hand, the effect of temperature on the mechanical response of the workpiece material is taken into account through the use of a temperature-dependent workpiece material model.

**3.1.3 Initial Conditions.** The Eulerian sub-domain is initially filled with the workpiece and the flow-visualization marker materials by prescribing the appropriate material

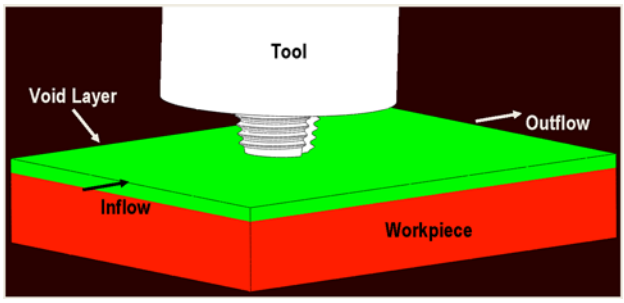


**Fig. 4** A schematic of a typical FSW tool (Lagrangian domain) and workpiece (Eulerian domain) used in the present work

volume fractions to each Eulerian element. To enable the motions of the Eulerian materials at the workpiece upper surface in the outward normal direction (without material loss), one or more top Eulerian element layers is initially left void. For the Lagrangian sub-domain, at the beginning of the analysis the tool is assigned a constant rotational velocity and a zero translational velocity. Both the Eulerian and Lagrangian sub-domains are assigned ambient-temperature initial conditions.

**3.1.4 Boundary Conditions.** For convenience, the longitudinal motion of the FSW tool is not considered explicitly. Instead, the longitudinal velocity of the tool is set to zero and the workpiece material is allowed to move through the Eulerian sub-domain with an overall longitudinal velocity equal to negative of the tool translational velocity. This was accomplished through the use of the appropriate "in-flow" and "out-flow" velocity boundary conditions over the vertical faces of the Eulerian domains which are orthogonal to the direction of tool travel. Thus, the Eulerian sub-domain displayed in Fig. 4 does not represent the entire workpiece but rather a rectangular region around the tool in the otherwise infinitely-long workpiece.

"No-flow" boundary conditions are prescribed along the Eulerian sub-domain vertical faces parallel to the tool travel direction to account for the role of the workpiece base-metal material in restraining material flow in the transverse direction. To mimic the role played by the workpiece rigid backing plate in preventing the flow of the workpiece material in the downward direction, zero normal velocity boundary conditions are applied over the bottom surface of the Eulerian sub-domain. In accordance with the initial conditions prescribed to the top Eulerian-element layers, "out-flow" boundary conditions are prescribed over the top surface of the Eulerian sub-domain.

As far as the thermal boundary conditions are concerned, standard convective boundary conditions are applied over free surfaces of the workpiece and the tool while enhanced convection boundary conditions are applied over the bottom face of the workpiece (to mimic the effect of enhanced heat extraction through the workpiece backing plate).

**3.1.5 Tool/Workpiece Contact Interactions.** Since the Eulerian and Lagrangian domains do not possess conformal meshes, the contact interfaces between the two could not be defined using mesh-based surfaces. Instead, contact interfaces between the Lagrangian and the Eulerian sub-domains are determined using the so-called "immersed boundary method" (Ref 31) which identifies, during each computational time increment, the boundary of the Eulerian sub-domain region which is occupied by the Lagrangian sub-domain. Eulerian-Lagrangian contact constraints are enforced using a penalty method, within which the extent of contact pressure is governed by the local surface penetrations (where the default penalty stiffness parameter is automatically maximized subject to stability limits). As far as the shear stresses are concerned they are transferred via a "slip/stick" algorithm that is shear stresses lower than the frictional shear stress are transferred without interface sliding (otherwise interface sliding takes place). The frictional shear stress is defined by a modified Coulomb law within which there is an upper limit to this quantity (set equal to the shear strength of the workpiece material). The frictional shear stress is then defined as a smaller of the product between the static/kinetic friction coefficient and the contact pressure, on one hand, and the workpiece material shear strength, on the other.

In addition to the Eulerian-Lagrangian contacts, interactions (of a "sticky" character) also occur between different Eulerian materials. This type of interaction is a consequence of the kinematic constraint which requires that all Eulerian materials residing in a single Eulerian element are subjected to the same strain. The Eulerian-Eulerian contacts allow normal (tensile and compressive) stresses to be transferred between adjoining materials while no slip at the associated material boundaries is allowed.

**3.1.6 Heat-Generation and Partitioning.** As mentioned earlier, both plastic deformation and frictional sliding are treated as heat sources. To account for the fact that a small fraction of the plastic-deformation work is stored in the form of crystal defects, 95% of this work was assumed to be dissipated in the form of heat. As far as heat generation due to frictional sliding is concerned, it is assumed that its rate scales with the product of local interfacial shear stress and the sliding rate, and that 100% of this energy is dissipated in the form of heat. Partitioning of this heat between the tool and the workpiece is then computed using the algorithm reported in Ref 32 and the appropriate thermal properties of the workpiece and tool materials.

**3.1.7 Computational Algorithm.** As mentioned earlier, a new CEL-based finite element analysis of the FSW process is developed. Within this analysis, the workpiece is treated as an Eulerian sub-domain, the tool is treated as a Lagrangian sub-domain and the interaction between the two is treated using an

**Table 1 Johnson-Cook yield strength ($\sigma_y$) material model parameters* and the corresponding elastic and thermal parameters for AA5059-H131**

| Parameter | Symbol | Units | Value |
|---|---|---|---|
| Reference strength | $A$ | MPa | 167.0 |
| Strain-hardening parameter | $B$ | MPa | 596.0 |
| Strain-hardening exponent | $n$ | N/A | 0.551 |
| Strain-rate coefficient | $C$ | N/A | 0.001 |
| Room temperature | $T_{\text{room}}$ | K | 293 |
| Melting temperature | $T_{\text{melt}}$ | K | 893.0 |
| Temperature exponent | $m$ | N/A | 1.0 |
| Young's modulus | $E$ | GPa | 70 |
| Poisson's ratio | $\nu$ | N/A | 0.3 |
| Density | $\rho$ | kg/m$^3$ | 2700 |
| Thermal conductivity | $k$ | W/m·K | 120 |
| Specific heat | $c_p$ | J/kg·K | 880 |

* $\sigma_y = \left[A + B\left(\bar{\varepsilon}^{pl}\right)^n\right]\left[1 + C\log\left(\dot{\bar{\varepsilon}}^{pl}/\dot{\bar{\varepsilon}}^{pl}_o\right)\right]\left[1 - T_H^m\right]$; $T_H = (T - T_{\text{room}})/(T_{\text{melt}} - T_{\text{room}})$

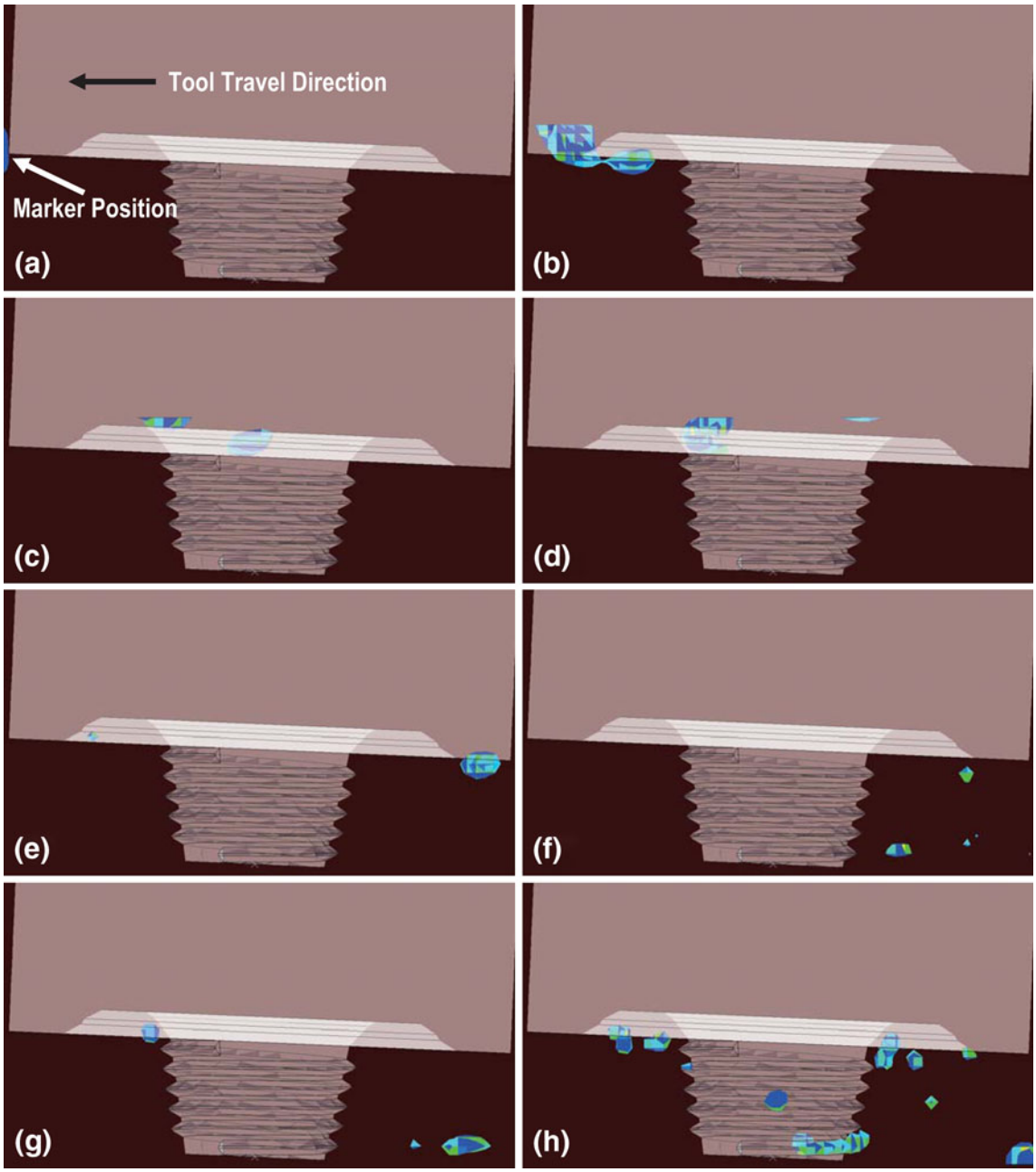


**Fig. 5** Side view of the spatial distribution and temporal evolution of the marker-material (initially located on the workpiece advancing-side/top-layer) volume fraction: tool rotation speed = 500 rpm; tool travel speed = 0.0025 m/s; tool tilt angle = 2.5°; tool plunge depth = 0.0001 m; 10 mm upper-diameter tool pin; welding time in seconds: (a) 2.7, (b) 6.6, (c) 10.5, (d) 14.4, (e) 18.3, (f) 22.2, (g) 26.1, (h) 30

Eulerian/Lagrangian contact (''fluid-structure interaction'') algorithm. Within the Lagrangian sub-domain: (a) The mesh (nodes and elements) is attached to the associated material and moves and deforms with it; and (b) each element must be fully filled with a single material. On the other hand, within an Eulerian sub-domain: (a) The mesh is fixed in space and the material flows through it; (b) elements are allowed to be partially filled and/or contain multiple materials; and (c) since the material and the element boundaries do not generally coincide, a separate (''interface reconstruction'') algorithm must be used to track the position of Eulerian material boundaries. The interface reconstruction algorithm approximates the material boundaries within an element as simple planar facets and, hence, accurate determination of a material's location within an element requires the use of fine Eulerian meshes.

Numerical solution of the governing equations in the Eulerian sub-domain within each time increment involves two separate steps: (a) the Lagrangian step within which the sub-domain is temporarily treated as being of a Lagrangian-type (i.e., nodes and elements are attached to and move/deform with the material); and (b) the ''remap'' step within which the distorted mesh is mapped onto the original Eulerian mesh and the accompanying material transport is computed and used to update the Eulerian-material states and inter-material boundaries.

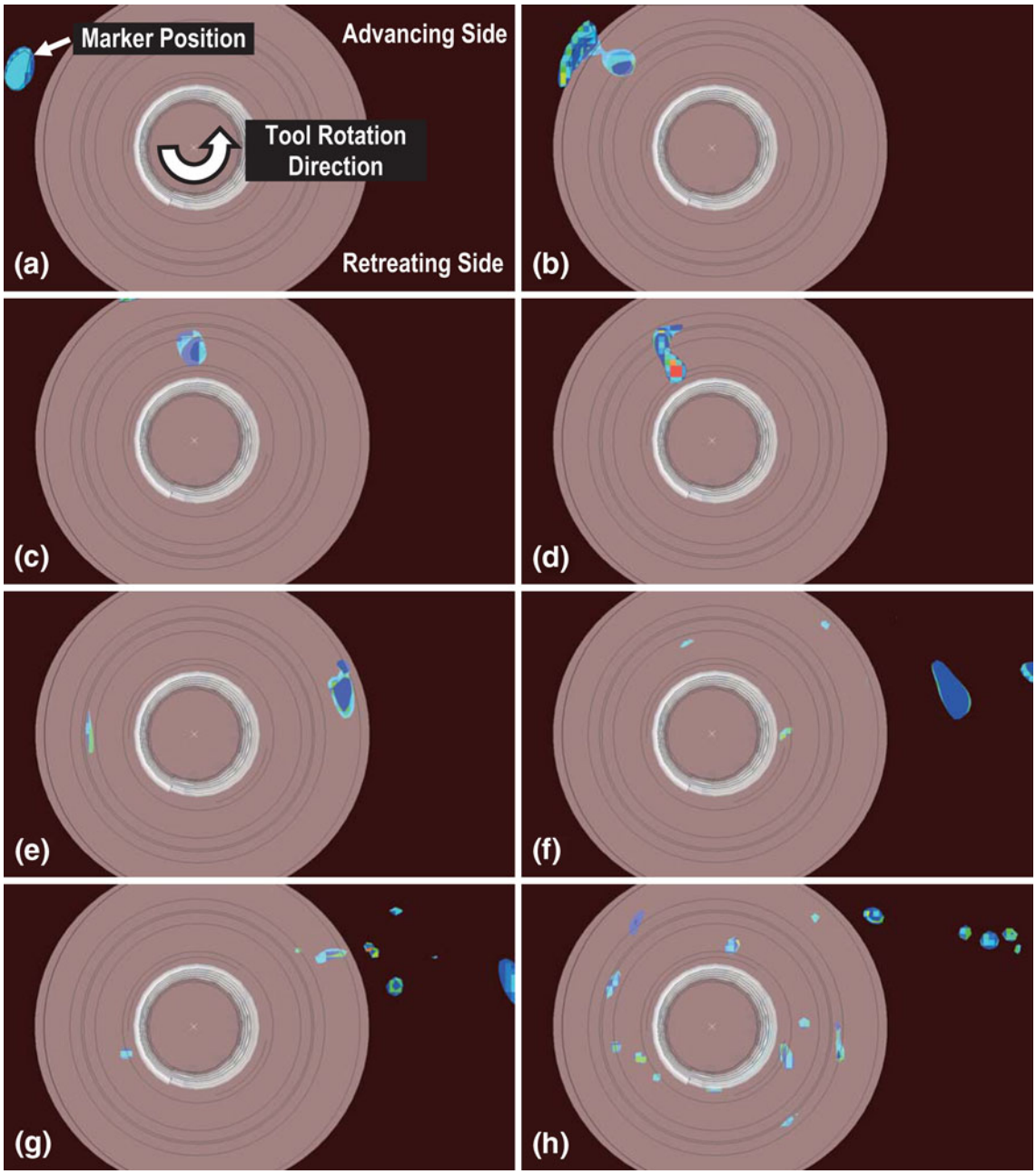


**Fig. 6** Top view of the spatial distribution and temporal evolution of the marker-material (initially located on the workpiece advancing-side/top-layer) volume fraction: tool rotation speed = 500 rpm; tool travel speed = 0.0025 m/s; tool tilt angle = 2.5°; tool plunge depth = 0.0001 m; 10 mm upper-diameter tool pin; welding time in seconds: (a) 2.7, (b) 6.6, (c) 10.5, (d) 14.4, (e) 18.3, (f) 22.2, (g) 26.1, (h) 30

It should be noted that the main reasons for using the CEL approach is that the conventional Lagrangian finite element analysis: (a) Does not allow material mixing within individual finite elements; and (b) becomes inaccurate and failure-prone when the elements experience a large degree of distortion.

The fully coupled thermo-mechanical problem dealing with FSW is solved using an explicit solution algorithm implemented in ABAQUS/Explicit (Ref 31), a general purpose finite element solver.

**3.1.8 Computational Accuracy, Stability, and Cost.** A standard mesh sensitivity analysis was carried out (the results not shown for brevity) to ensure that the results obtained are accurate, i.e., insensitive to the size of the elements used.

Due to the conditionally stable nature of the explicit finite element analysis used, the maximum time increment during each computational step had to be lower than the attendant stable time increment. To keep the computational cost reasonable while ensuring accuracy and stability of the computational procedure, a mass scaling algorithm is used. This algorithm adaptively adjusts material density in the critical stable time-increment controlling finite elements without significantly affecting the computational analysis results. A typical 30 s FSW computational analysis required 10-h of (wall-clock) time on a 12 core, 3.0 GHz machine with 16 GB of memory.

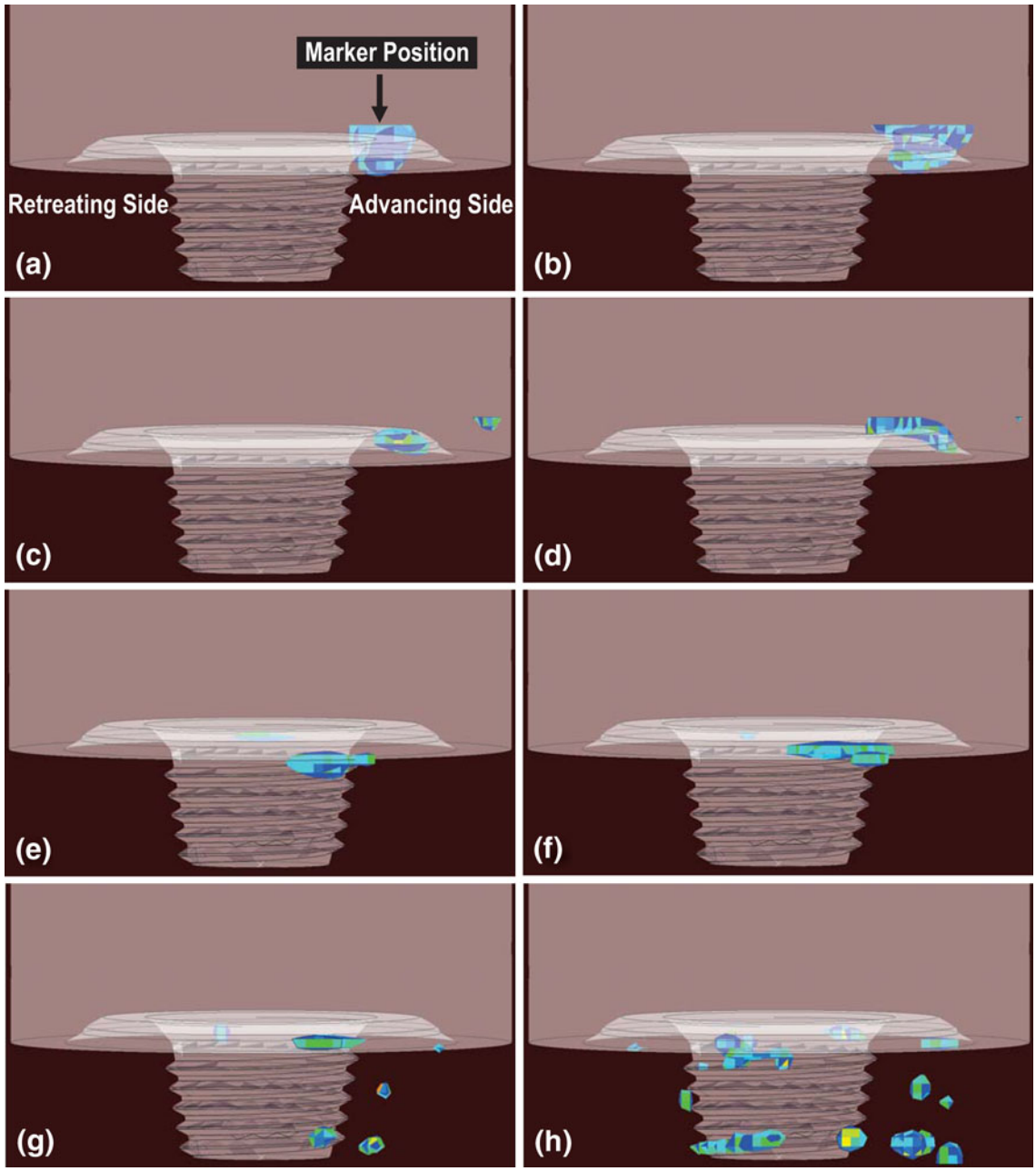


**Fig. 7** Rear view of the spatial distribution and temporal evolution of the marker-material (initially located on the workpiece advancing-side/top-layer) volume fraction: tool rotation speed = 500 rpm; tool travel speed = 0.0025 m/s; tool tilt angle = 2.5°; tool plunge depth = 0.0001 m; 10 mm upper-diameter tool pin; welding time in seconds: (a) 2.7, (b) 6.6, (c) 10.5, (d) 14.4, (e) 18.3, (f) 22.2, (g) 26.1, (h) 30

### *3.2 Material Models*

**3.2.1 Tool Material.** FSW tools used for joining aluminum alloys are typically made of one of the hot-working or high-speed steel grades (e.g., AISI H13 or AISI 350M). Due to high strength of these steel grades at elevated temperatures, the tool typically experiences very little plastic deformation during the FSW process. On the other hand, tool wear and loss of tool features after prolonged use is frequently observed. Since an analysis of tool wear is beyond the scope of the present work and the likely hood for plastic deformation of the tool is very small, the tool material (AISI H13) is modeled as a mechanically isotropic linear-elastic material with a Young's Modulus of 210 GPa, a Poisson's ratio of 0.3, and density of 7825 kg/m$^3$. The thermal properties of this material which play an important role in partitioning of frictional-sliding-induced heat at the tool/workpiece interface are assigned as: thermal conductivity, $k$ = 28.5 W/m · K and specific heat, $c_p$ = 475 J/kg · K.

**3.2.2 Workpiece Material.** The workpiece material (AA5059-H131, a solid-solution strengthened and strain-hardened/stabilized Al-Mg-Mn alloy) is assumed to be isotropic, linear-elastic and strain-hardenable, strain-rate sensitive, thermally softenable plastic material and is modeled using the Johnson-Cook material model (Ref 33). A summary of the

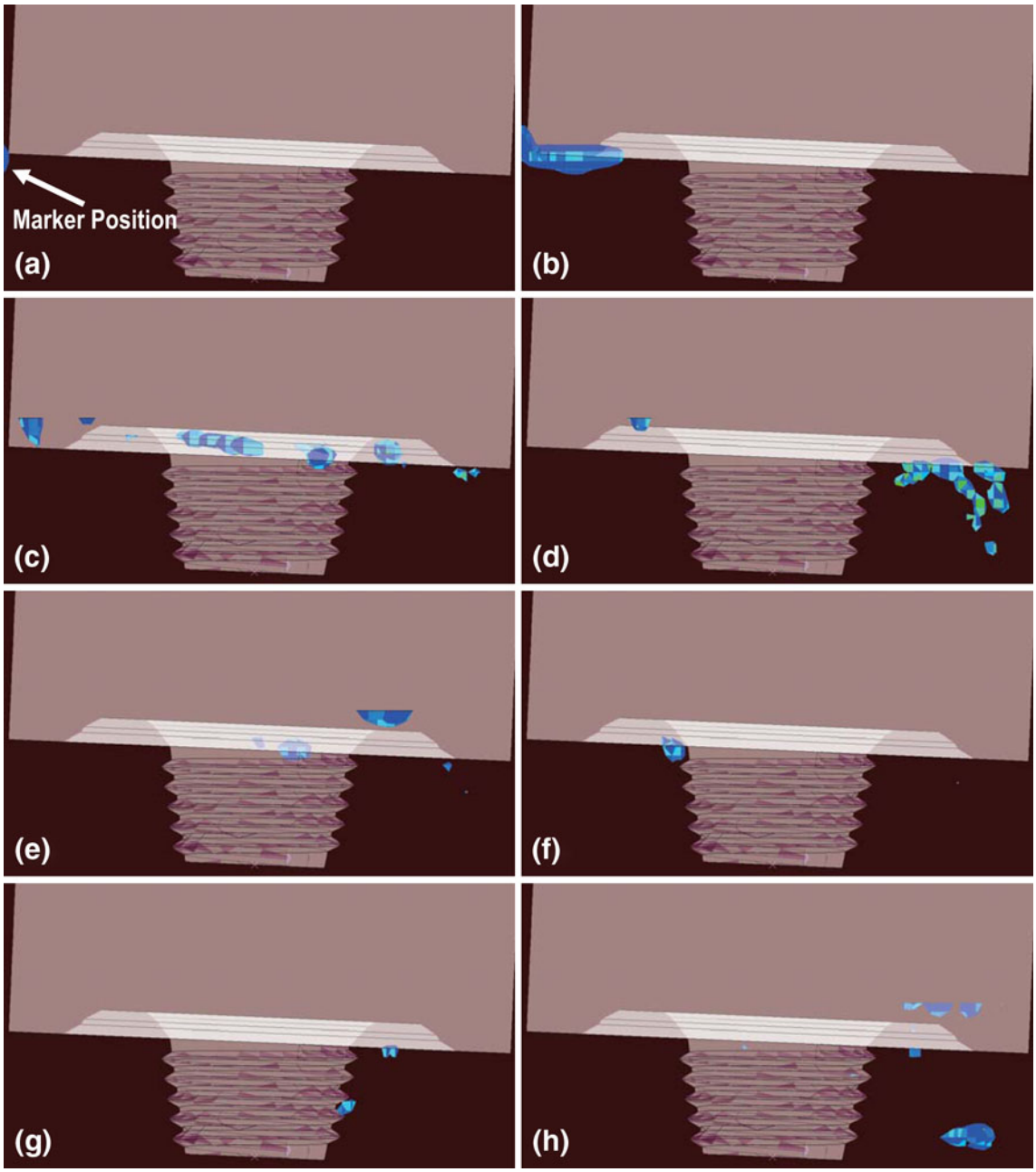


**Fig. 8** Side view of the spatial distribution and temporal evolution of the marker-material (initially located on the workpiece interface/top-layer) volume fraction: tool rotation speed = 500 rpm; tool travel speed = 0.0025 m/s; tool tilt angle = 2.5°; tool plunge depth = 0.0001 m; 10 mm upper-diameter tool pin; welding time in seconds: (a) 2.7, (b) 6.6, (c) 10.5, (d) 14.4, (e) 18.3, (f) 22.2, (g) 26.1, (h) 30

Johnson-Cook material model parameters (including the yield stress, $\sigma_y$, governing equation) and the elastic and thermal properties of AA5059-H131 are provided in Table 1.

Examination of the original Johnson-Cook material model reveals that a temperature change causes only a reversible change in material strength by affecting thermal activation of dislocation motion. In other words, the original Johnson-Cook model does not account for any permanent changes in the material microstructure and properties which may occur as a result of high-temperature exposure of the material. This approach is not fully justified in the case of FSW where, due to the attendant high temperatures, significant differences in the material microstructure and properties may exist between the base metal and the weld (as well as within different regions of the weld). To account for this additional effect of temperature, a modification of the strain hardening term within the original Johnson-Cook model was proposed in our prior work (Ref 20). Specifically, the strain hardening term is still assumed to be a parabolic function of equivalent plastic strain ( $B\bar{\varepsilon}_{pl}^{n}$, where $B$ and $n$ are material parameters, Table 1). However, the equivalent plastic strain, $\bar{\varepsilon}_{pl}$, is now defined as the sum of two terms: one (positive) which quantifies the contribution of plastic deformation to strain hardening and the other (negative) which accounts for strain softening induced by dynamic recrystallization. In other words, strain hardening is still assumed to be controlled by the density of (mobile) dislocations but the local

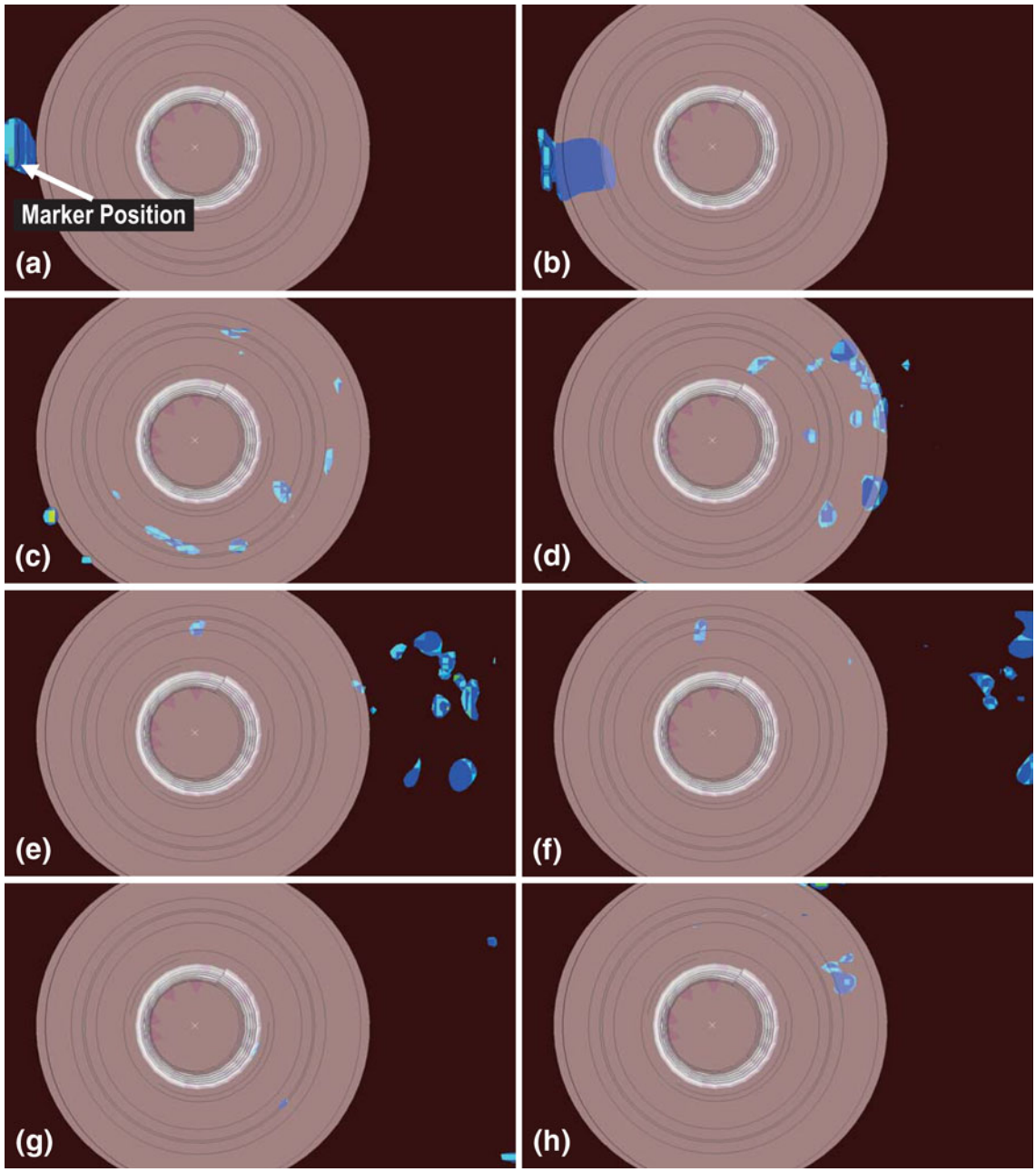


**Fig. 9** Top view of the spatial distribution and temporal evolution of the marker-material (initially located on the workpiece interface/top-layer) volume fraction: tool rotation speed = 500 rpm; tool travel speed = 0.0025 m/s; tool tilt angle = 2.5°; tool plunge depth = 0.0001 m; 10 mm upper-diameter tool pin; welding time in seconds: (a) 2.7, (b) 6.6, (c) 10.5, (d) 14.4, (e) 18.3, (f) 22.2, (g) 26.1, (h) 30

value of this quantity is taken to be the result of a competition between dislocation-generating plastic deformation and dislocation annihilation associated with dynamic recrystallization. It should be noted that the first (positive) component of the equivalent plastic strain in the modified Johnson-Cook material model still quantifies the overall extent of inelastic deformation taking place at a given material point.

## 4. Results and Discussion

As mentioned earlier, the main objective of the present work is to study the flow of the workpiece material during FSW and to correlate this flow with the values/levels of the friction stir welding process key parameters. Toward that end, a marker was placed (on either the advancing or retreating workpiece sides, or along the weld interface) along the path of the advancing FSW tool. The marker material was identical to the remainder of the workpiece material. However, by declaring the marker material as a different material within the Eulerian region, it was possible to monitor the flow of the workpiece material during the FSW process and to assess the extent of material mixing during FSW.

To help with the visualization of the marker material flow, the volume fraction of the marker material within the Eulerian cells was monitored. At the beginning of the simulation, each marker

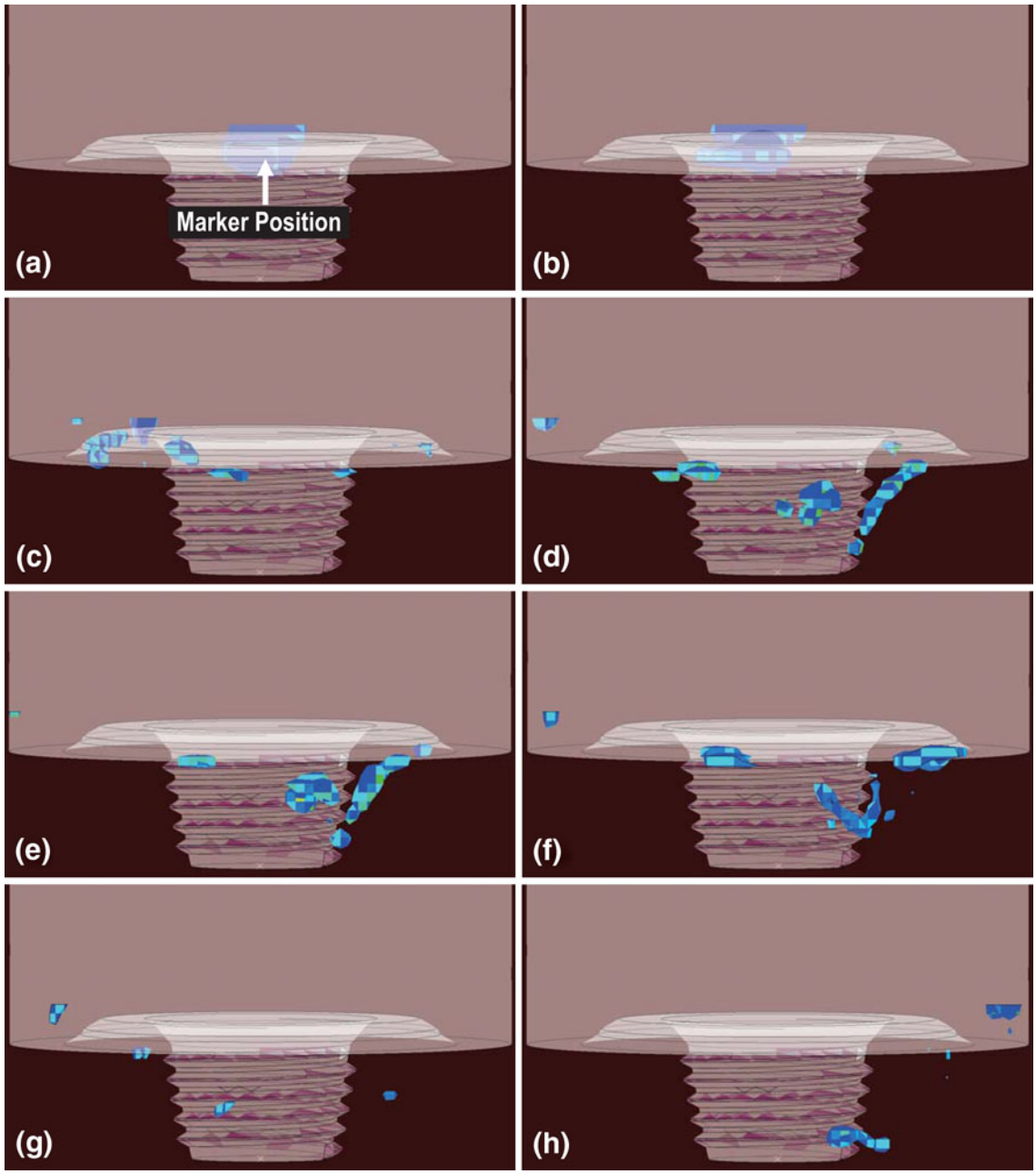


**Fig. 10** Rear view of the spatial distribution and temporal evolution of the marker-material (initially located on the workpiece interface/top-layer) volume fraction: tool rotation speed = 500 rpm; tool travel speed = 0.0025 m/s; tool tilt angle = 2.5°; tool plunge depth = 0.0001 m; 10 mm upper-diameter tool pin; welding time in seconds: (a) 2.7, (b) 6.6, (c) 10.5, (d) 14.4, (e) 18.3, (f) 22.2, (g) 26.1, (h) 30

(one marker was used in a single analysis) contained hundred percent of the marker material (i.e., the volume fraction of the marker material within the marker was initially 1.0). However, as the friction stir welding process simulation proceeded, due to the flow of the marker material and its mixing with the remainder of the workpiece material, the marker material spread over a wider region. At the same time, in accordance with the mass conservation requirement, as the marker material was spread over a wider region the volume fraction of the marker material experienced a continues decrease.

To further help visualize the material flow during FSW, the workpiece material is not shown in the figures displayed in this section. Only the marker material distribution/volume fraction is displayed (in addition to that of the friction stir welding tool). Also, the friction stir welding tool was made partially transparent so that the location of the marker material under the friction stir welding tool shoulder can be monitored.

In this section, the results of the material flow analysis are presented and discussed. The results are presented in the following way: First, a base line case is considered within which a prototypical set of friction stir welding process parameters was chosen. This is followed by a section in which the effect of variation of few specific FSW process parameters was investigated.

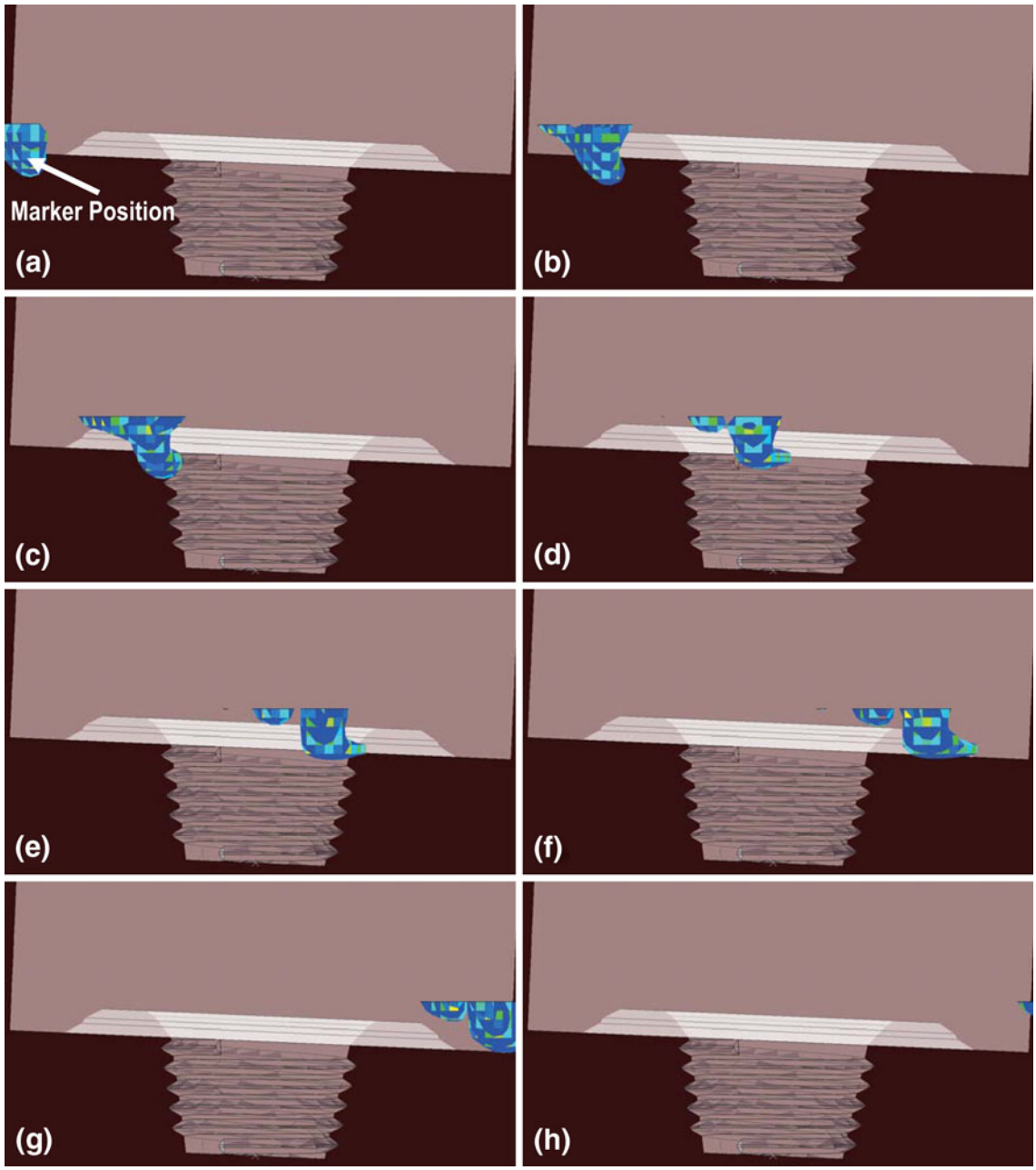


**Fig. 11** Side view of the spatial distribution and temporal evolution of the marker-material (initially located on the workpiece retreating side/top-layer) volume fraction: tool rotation speed = 500 rpm; tool travel speed = 0.0025 m/s; tool tilt angle = 2.5°; tool plunge depth = 0.0001 m; 10 mm upper-diameter tool pin; welding time in seconds: (a) 3.9, (b) 5.4, (c) 7.2, (d) 8.4, (e) 9.9, (f) 11.4, (g) 12.9, (h) 14.4

### *4.1 Baseline Case*

In this section, prototypical values/levels are assigned to the FSW key process parameters. Specifically: (a) tool geometry: (i) tool shoulder diameter = 0.025 m, (ii) FSW tool shoulder truncated conical under-cut angle = 7°, (iii) pin length = 0.0057 m, (iv) pin upper diameter = 0.01 m, (v) pin-taper angle = 10°, and (vi) pin thread pitch = 800 threads/m; (b) tool material = AISI H13 tool steel; (c) workpiece material = AA5059; (d) tool rotation speed = 500 rpm; (e) tool travel speed = 0.0025 m/s; (f) tool tilt angle = 2.5°, and (g) tool plunge depth = 0.0001 m.

Spatial distribution and temporal evolution of the volume fraction of the marker material for the base line case in which the marker was placed on the advancing side of the workpiece are depicted in Fig. 5(a) to (h). The results displayed in these figures represent a side view in which the tool is traveling to the left (relative to the workpiece material). The corresponding top and rear (behind the tool) views of the same results are, respectively, displayed in Fig. 6(a) to (h) and 7(a) to (h), respectively.

The corresponding baseline case results in the three views for the case when the marker was placed at the welding interface are displayed in Fig. 8(a) to (h), 9(a) to (h), and 10(a) to (h).

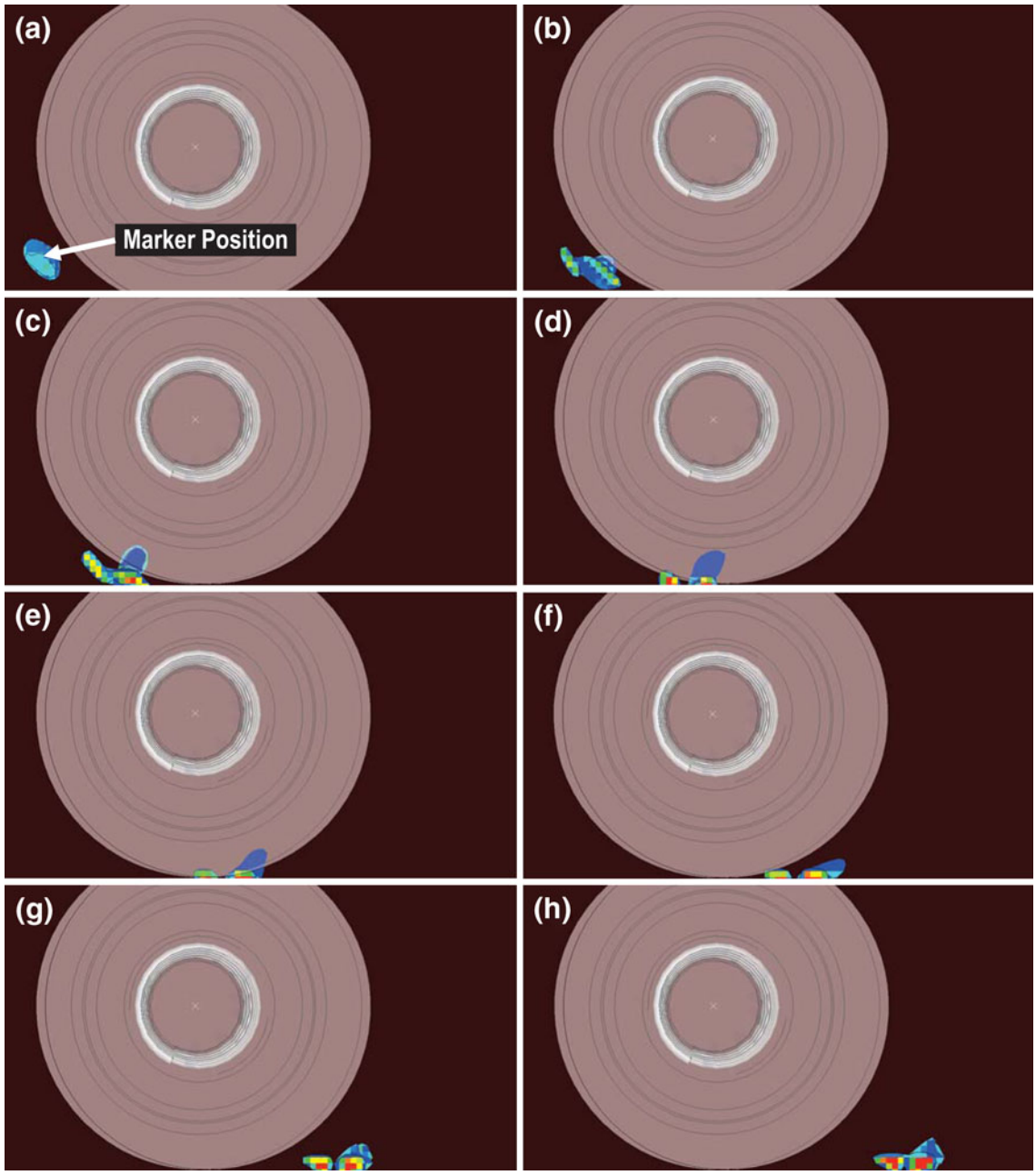


**Fig. 12** Top view of the spatial distribution and temporal evolution of the marker-material (initially located on the workpiece retreating side/top-layer) volume fraction: tool rotation speed = 500 rpm; tool travel speed = 0.0025 m/s; tool tilt angle = 2.5°; tool plunge depth = 0.0001 m; 10 mm upper-diameter tool pin; welding time in seconds: (a) 3.9, (b) 5.4, (c) 7.2, (d) 8.4, (e) 9.9, (f) 11.4, (g) 12.9, (h) 14.4

Likewise, the corresponding results for the case when the marker was placed on the retreating side of the workpiece are shown in Fig. 11(a) to (h), 12(a) to (h), and 13(a) to (h), respectively.

It should be noted that the results presented in Fig. 5(a) to (h) to 13(a) to (h) correspond to the cases when the marker was placed at the top surface of the workpiece (as labeled in part (a) of these figures). Within the present work, the workpiece configurations in which the marker was placed half way through the workpiece thickness or near the bottom-surface of the workpiece were also analyzed. Since these results were qualitatively similar to the ones presented here (although they showed a decrease in the extent of material mixing), they will not be presented here.

Examination of the results presented in Fig. 5(a) to (h) to 13(a) to (h) revealed that:

(a) While the marker material was initially confined within a cubic domain (the initial configuration is not shown for brevity), due to its flow and mixing with the surrounding workpiece material, it became dispersed over a larger spatial domain of the workpiece. At the same time, the volume fraction of the marker material decreased, in accordance with the mass conservation requirements;
(b) At the completion of the FSW process, the marker material tends to reside on the same side of the welding interface as that where it was originally placed (e.g., the

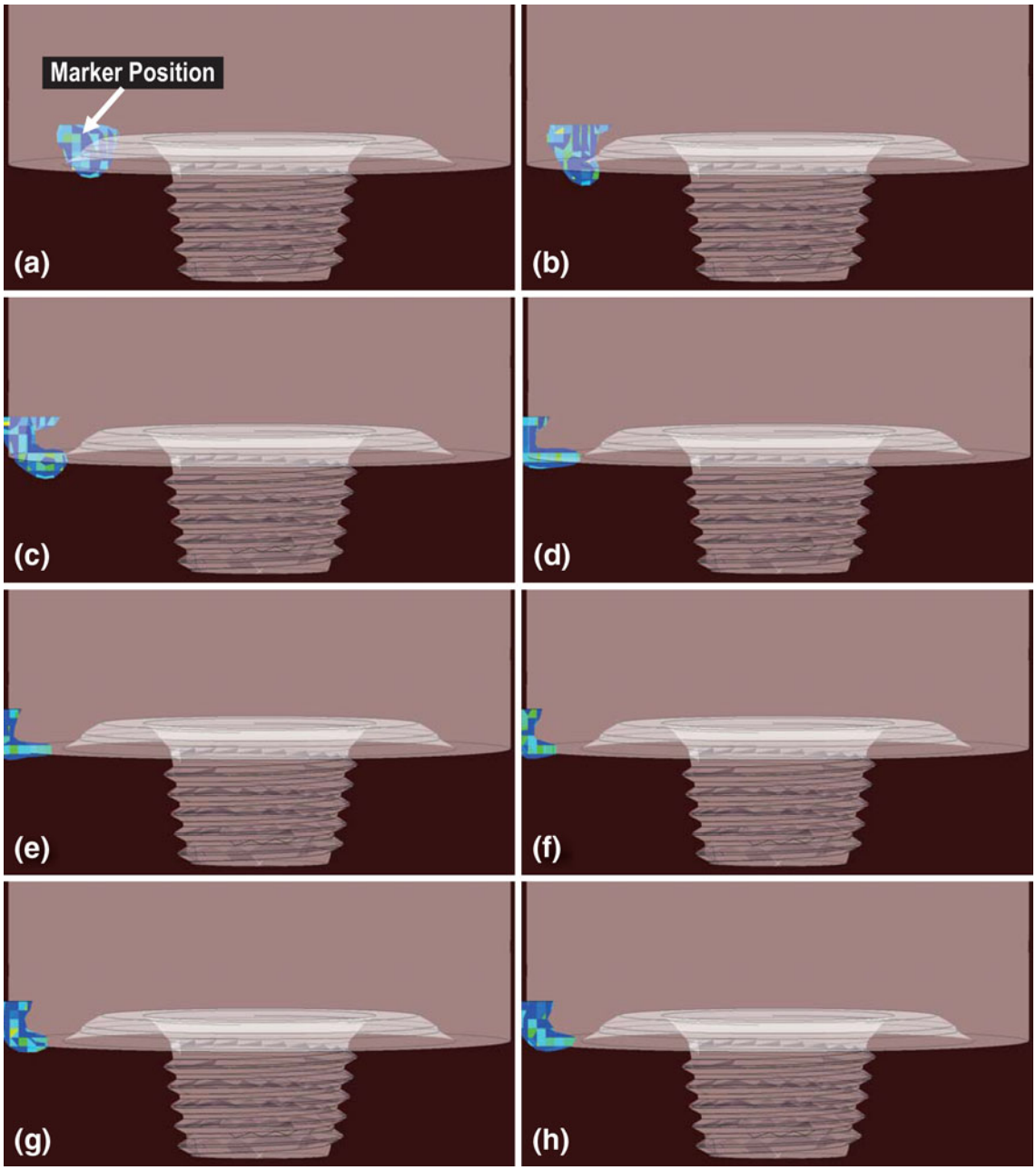


**Fig. 13** Rear view of the spatial distribution and temporal evolution of the marker-material (initially located on the workpiece retreating side/top-layer) volume fraction: tool rotation speed = 500 rpm; tool travel speed = 0.0025 m/s; tool tilt angle = 2.5°; tool plunge depth = 0.0001 m; 10 mm upper-diameter tool pin; welding time in seconds: (a) 3.9, (b) 5.4, (c) 7.2, (d) 8.4, (e) 9.9, (f) 11.4, (g) 12.9, (h) 14.4

advancing side marker-material is ultimately placed in the advancing side weld region). However, it should be noted that this process is accompanied by a considerable dispersion of the marker material in both the lateral and through-the-thickness directions;

(c) For the most part, FSW causes the workpiece material flow in the horizontal plane (a plane parallel with the workpiece backing plate), e.g. Fig. 5(b) to (d). In addition (downward) flow of the marker material in the through-the-thickness direction was also observed. In the case of the advancing-side marker, this component of the material flow was fairly pronounced, Fig. 5(h) and 7(h). This component of the material flow still exists but is less pronounced in the case of the weld-interface marker, Fig. 8(h) and 10(h). On the other hand, practically no marker material flow in the through-the-thickness direction occurs in the case of the retreating-side marker, Fig. 11(h) and 13(h);

(d) The material downward flow is, at least partly, promoted by the threaded-pin auguring effect, e.g., Fig. 8(f) and (g);

(e) The extent of marker-material dispersion is highest in the case of the advancing side marker, Fig. 6(h). It is intermediate in the case of the weld-interface marker and the lowest in the case of the retreating-side marker. In other words, the advancing material undergoes extensive

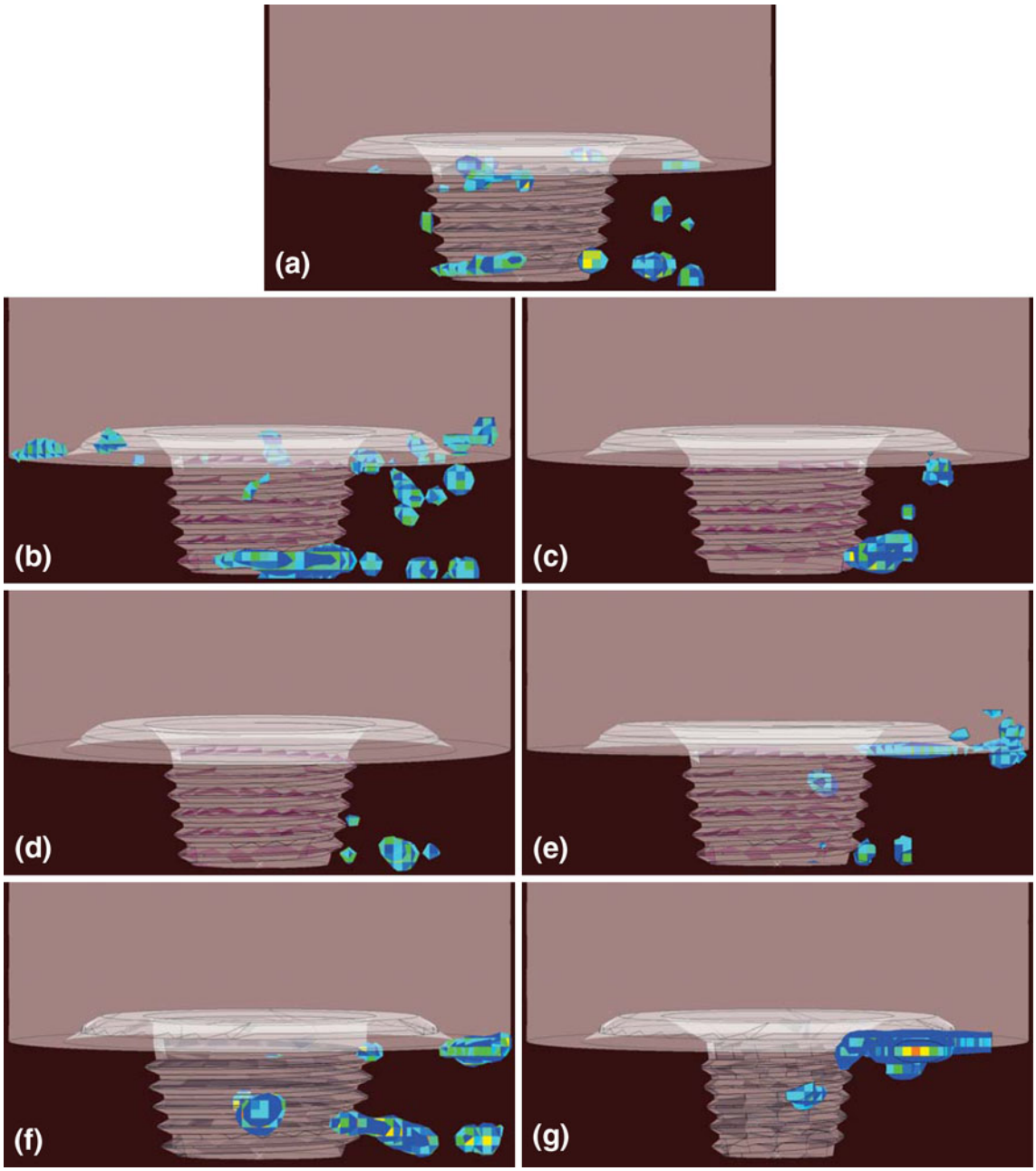


**Fig. 14** Rear view of the spatial distribution of the marker-material (initially located on the workpiece advancing-side/top-layer) volume fraction for: (a) baseline case, tool rotation speed = 500 rpm, tool travel speed = 0.0025 m/s, tool plunge depth = 0.0001 m, tool tilt angle = 2.5°, 10 mm upper-diameter tool pin; (b) tool rotation speed = 700 rpm; (c) tool rotation speed = 300 rpm; (d) tool tilt angle = 3.50°; (e) tool tilt angle = 2.0°; (f) 12 mm upper-diameter tool pin; and (g) 8 mm upper-diameter tool pin. Note that for cases (b) to (g) the values of the unspecified FSW parameters are the same as in the baseline case (a)

stirring before it is ultimately placed into the weld. In sharp contrast, the retreating-side marker material is mainly extruded around the tool and forged in the wake of the tool (without experiencing substantial mixing); and

(f) There is no evidence for rotation of the marker material around the welding direction in any of the results being analyzed. That is, no instances of marker material crossing from the advancing to the retreating side were observed at the lower portion of the workpiece and in the wake of the FSW tool as suggested by the experimental results of Reynolds and co-workers (Ref 27-30).

### 4.2 The Effect of FSW-Process Parameters on Workpiece Material Flow

Within the present work, the effect of the following FSW process parameters on the workpiece material flow has been investigated: (a) Weld pitch (defined as the ratio of the FSW tool travel speed to the tool rotation speed); (b) tool tilt-angle; and (c) the tool pin upper and lower diameters (at a constant pin taper angle). In all the simulations presented in this section, only one of these process parameters was altered (i.e., all the remaining process parameters were kept unchanged relative to their baseline counterparts). To help in revealing the effect of these

process parameters on the workpiece material flow, the rear-view, end-of-the-simulation, advancing-side, marker-material volume fraction results for the base-line case are displayed in Fig. 14(a). A comparison of the results displayed in Fig. 14(a) with the results displayed in the remaining parts of Fig. 14 are used to infer the effect of the specific FSW process parameters.

**4.2.1 Weld Pitch.** The effect of the weld pitch can be inferred by comparing the results displayed in Fig. 14(b), (a), and (c), respectively. The magnitudes of the weld pitch in these three cases are: $3.41 \times 10^{-5}$ m/radian, $4.77 \times 10^{-5}$ m/radian, and $7.95 \times 10^{-5}$ m/radian, respectively. Examination of the results displayed in these figures reveals that the highest extent of marker-material mixing/dispersion is attained at the lowest value of the weld pitch, Fig. 14(b) and this extent continuously decreases with an increase in the magnitude of the weld pitch, Fig. 14(a) and (c). This finding is expected since a lower value of the weld pitch (i.e., an increased tool rotational speed at a constant tool travel speed) represents an increase in the mechanical energy introduced into the workpiece through the rotating FSW tool. Dissipation of this energy in the form of heat increases the workpiece temperature, softens the workpiece material and, hence, facilitates material mixing.

**4.2.2 Tool Tilt-Angle.** The effect of the tool tilt-angle can be inferred by comparing the results displayed in Fig. 14(d), (a), and (e), respectively. The magnitudes of the tool tilt-angle in these three cases are: 3.5°, 2.5°, and 2.0°, respectively. Examination of the results displayed in these figures reveals that the highest extent of marker-material mixing/dispersion is attained in the baseline case, Fig. 14(a) and that this extent decreases with a deviation in the tilt-angle from its baseline value. In other words, a tilt-angle around the baseline value of 2.5° appears to be optimal. This finding is in accordance with the experimental observations in the FSW welding practice. The existence of an optimum tilt-angle is generally described as a trade-off between the maximization of the forging pressure (favors a large tilt-angle) and minimization of the workpiece-weld "ploughing" (favors a smaller tilt-angle). The present results show that maximization of workpiece-material stirring/mixing also favors an optimal value of the tilt-angle.

**4.2.3 Tool-Pin Upper and Lower Diameters.** The effect of the tool-pin size (as quantified by the upper and lower diameter(s)) at a constant value of the tool-pin taper angle of 10° can be inferred by comparing the results displayed in Fig. 14(f), (a), and (g), respectively. The tool-pin upper diameters in these three cases are: 0.012, 0.01, and 0.008 m, respectively. Examination of the results displayed in these figures clearly shows that the highest extent of marker-material mixing/dispersion is attained in the case of the largest pin size, Fig. 14(f) and that this extent decreases with a decrease in the pin size. This finding is in accordance with the experimental observations in the FSW welding practice and with the fact that the mechanical energy introduced into the workpiece through the rotating FSW tool increases with the tool pin size.

## 5. Summary and Conclusions

Based on the results presented and discussed in the present work, the following main summary remarks and conclusions can be made:

1. A coupled thermo-mechanical Eulerian/Lagrangian finite element analysis is carried out to investigate material flow and mixing during the Friction Stir Welding (FSW) process. Particular attention is paid to the effect of "weld pitch" (defined as a longitudinal advancement per single revolution of the tool), toot tilt-angle, and the tool pin size on the flow pattern and the extent of material mixing during FSW.
2. The results obtained show that FSW does not cause a large-scale permanent exchange of the workpiece material between the advancing and the retreating side, i.e., majority of the workpiece material within the weld resides on the workpiece side (advancing/retreating) on which it was located before welding.
3. For the most part, FSW causes the workpiece material flow in the horizontal plane (a plane parallel with the workpiece backing plate). In addition, downward through-the-thickness motion of the material and the accompanying mixing are found to be quite pronounced on the advancing workpiece side while this component of the material flow was not very prominent on the retreating side.
4. The desired maximum extent of material mixing has been found, within the explored ranges of FSW process parameters, to correspond to the minimum value of the weld pitch, an optimum value of the tool tilt-angle, and a maximum value of the tool pin-size. A simple rationale has been provided for these observations.


## Acknowledgments

The material presented in this paper is based on work supported by two Army Research Office sponsored Grants (W911NF-11-1-0207 and W911NF-09-1-0513) and two U.S. Army/Clemson University Cooperative Agreements (W911NF-04-2-0024 and W911NF-06-2-0042).


## References


1. W.M. Thomas, E.D. Nicholas, J.C. Needham, M.G. Murch, P. Temple-Smith, and C.J. Dawes, Friction Stir Butt Welding, International Patent Application No. PCT/GB92/02203 (1991)
2. C.J. Dawes and W.M. Thomas, Friction Stir Joining of Aluminum Alloys, *TWI Bull.*, 1996, **6**, p 124
3. H. Liu, H. Fulii, M. Maeda, and K. Nogi, Tensile Properties and Fracture locations of Friction-Stir Welded joints of 6061-T6 Aluminium Alloy, *J. Mater. Sci. Lett.*, 2003, **22**, p 1061–1063
4. W.B. Lee, C.Y. Lee, W.S. Chang, Y.M. Yeon, and S.B. Jung, Microstructural Investigation of Friction Stir Welded Pure Titanium, *Mater. Lett.*, 2005, **59**, p 3315–3318
5. W.M. Thomas and E.D. Nicholas, Friction Stir Welding for the Transportation Industries, *Mater. Des.*, 1997, **18**, p 269–273
6. J.Q. Su, T.W. Nelson, R. Mishra, and M. Mahoney, Microstructural Investigation of Friction Stir Welded 7050-T651 Aluminum, *Acta Mater.*, 2003, **51**, p 713–729
7. O. Frigaard, Ø. Grong, and O.T. Midling, A Process Model for Friction Stir Welding of Age Hardening Aluminum Alloys, *Metall. Mater. Trans. A*, 2001, **32**, p 1189–1200
8. M.W. Mahoney, C.G. Rhodes, J.G. Flintoff, R.A. Spurling, and W.H. Bingel, Properties of Friction-Stir-Welded 7075 T651 Aluminum, *Mater. Trans. A*, 7075, **29**(1998), p 1955–1964
9. C.G. Rhodes, M.W. Mahoney, W.H. Bingel, R.A. Spurling, and C.C. Bampton, Effect of Friction Stir Welding on Microstructure of 7075 Aluminum, *Scripta Mater.*, 1997, **36**, p 69–75
10. G. Liu, L.E. Murr, C.S. Niou, J.C. McClure, and F.R. Vega, Microstructural Aspects of the Friction-Stir-Welding of 6061-T6 Aluminum, *Scripta Mater.*, 1997, **37**, p 355–361
11. M. Grujicic, G. Arakere, C-F.Yen, and B.A. Cheeseman, Computational Investigation of Hardness Evolution during Friction-stir Welding

of AA5083 and AA2139 aluminum alloys, *J. Mater. Eng. Perform.*, 2010. doi:10.1007/s11665-010-9741-y

12. M.Z.H. Khandkar, J.A. Khan, and A.P. Reynolds, Prediction of Temperature Distribution and Thermal History During Friction Stir Welding: Input Torque Based Model, *Sci. Technol. Weld. Join.*, 2003, **8**, p 165–174
13. S. Xu, X. Deng, A.P. Reynolds, and T.U. Seidel, Finite Element Simulation of Material Flow in Friction Stir Welding, *Sci. Technol. Weld. Join.*, 2001, **6**, p 191–193
14. K.V. Jata and S.L. Semiatin, Continuous Dynamic Recrystallization During Friction Stir Welding, *Scripta Mater.*, 2000, **43**, p 743–748
15. R. Nandan, G.G. Roy, and T. DebRoy, Numerical Simulation of Three-Dimensional Heat Transfer and Plastic Flow During Friction Stir Welding, *Metall. Mater. Trans. A*, 2006, **37**, p 1247–1259
16. R. Nandan, G.G. Roy, and T. DebRoy, Three-Dimensional Heat and Material Flow During Friction Stir Welding of Mild Steel, *Acta Mater.*, 2007, **55**, p 883–895
17. R. Nandan, T.J. Lienert, and T. DebRoy, Toward Reliable Calculations of Heat And Plastic Flow During Friction Stir Welding of Ti-6Al-4V Alloy, *Int. J. Mater. Res.*, 2008, **99**, p 434–444
18. H. Schmidt, T.L. Dickerson, and J. Hattel, Material Flow in Butt Friction Stir Welds In AA2024-T3, *Acta Mater.*, 2006, **54**, p 1199–1209
19. L. Fratini, G. Buffa, D. Palmeri, J. Hua, and R. Shivpuri, Material Flow in FSW of AA7075-T6 Butt Joints: Numerical Simulations and Experimental Verifications, *Sci. Technol. Weld. Join.*, 2006, **11**, p 412–421
20. M. Grujicic, T. He, G. Arakere, H.V. Yalavarthy, C.-F. Yen, and B.A. Cheeseman, Fully-Coupled Thermo-Mechanical Finite-element Investigation of Material Evolution During Friction-Stir Welding of AA5083, *J. Eng. Manuf.*, 2010, **224**(4), p 609–625
21. M. Grujicic, G. Arakere, H.V. Yalavarthy, T. He, C.-F. Yen, and B.A. Cheeseman, Modeling of AA5083 Material-Microstructure Evolution During Butt Friction-Stir Welding, *J. Mater. Eng. Perform.*, 2010, **19**(5), p 672–684
22. M. Grujicic, G. Arakere, B. Pandurangan, A. Hariharan, C.-F. Yen, B.A. Cheeseman, and C. Fountzoulas, Computational Analysis and Experimental Validation of the Ti-6Al-4V Friction Stir Welding Behavior, *J. Eng. Manuf.*, 2010, **224**(8), p 1–16
23. M. Grujicic, G. Arakere, A. Hariharan, and B. Pandurangan, A Concurrent Product-development Approach for Friction-stir Welded Vehicle-underbody Structures, *J. Eng. Manuf.*, 2011. doi:10.1007/s11665-011-9955-7
24. O.T. Midling, Material Flow Behavior and Microstructural Integrity of Friction Stir Butt Weldments, *Proc. 4th International Conf. on Aluminum Alloys, Atlanta, GA*, 1994
25. Y. Li, L.E. Murr, and J.C. McClure, Solid-State Flow Visualization in the Friction-Stir Welding of 2024 Al to 6061 Al, *Scripta Mater.*, 1999, **40**, p 1041–1046
26. K. Colligan, Material Flow Behavior During Friction Stir Welding of Aluminum, *Weld. J.*, 1999, **78**(7), p 229–237
27. A.P. Reynolds, T.U. Seidel, and M. Simonsen, Visualisation of Material Flow in an Autogenous Friction Stir Weld, *Proc. 1st International Symp. FSW, Thousand Oaks, CA*, 1999
28. A.P. Reynolds, Visualization of Material Flow in an Autogenous Friction Stir Weld, *Sci. Technol. Weld. Join.*, 2000, **5**, p 120–124
29. T.U. Seidel and A.P. Reynolds, *Proc. SECTAM, Pine Mountain, GA*, 2000
30. T.U. Seidel and A.P. Reynolds, Visualization of the Material Flow in AA2195 Friction-Stir Welds Using a Marker Insert Technique, *Metall. Mater. Trans. A*, 2001, **32**, p 2879–2884
31. ABAQUS Version 6.10EF, User Documentation, Dassault Systems, 2011
32. S. Xu, X. Deng, A.P. Reynolds, and T.U. Seidel, Finite Element Simulation of Material Flow in Friction Stir Welding, *Sci. Technol. Weld. Join.*, 2001, **6**, p 191–193
33. G.R. Johnson and W.H. Cook, A Constitutive Model and Data for Metals Subjected to Large Strains, High Strain Rates and High Temperatures, *Proceedings of the 7th International Symposium on Ballistics*, 1983